

Hydrodynamic thrust generation and power consumption investigations for piezoelectric fins with different aspect ratios

S. Shahab^a, D. Tan, and A. Erturk

G.W. Woodruff School of Mechanical Engineering, Georgia Institute of Technology,
Atlanta, GA 30332, USA

Received 14 July 2015 / Received in final form 2 November 2015
Published online 15 December 2015

Abstract. Bio-inspired hydrodynamic thrust generation using piezoelectric transduction has recently been explored using Macro-Fiber Composite (MFC) actuators. The MFC technology strikes a balance between the actuation force and structural deformation levels for effective swimming performance, and additionally offers geometric scalability, silent operation, and ease of fabrication. Recently we have shown that mean thrust levels comparable to biological fish of similar size can be achieved using MFC fins. The present work investigates the effect of length-to-width (L/b) aspect ratio on the hydrodynamic thrust generation performance of MFC cantilever fins by accounting for the power consumption level. It is known that the hydrodynamic inertia and drag coefficients are controlled by the aspect ratio especially for $L/b < 5$. The three MFC bimorph fins explored in this work have the aspect ratios of 2.1, 3.9, and 5.4. A nonlinear electrohydroelastic model is employed to extract the inertia and drag coefficients from the vibration response to harmonic actuation for the first bending mode. Experiments are then conducted for various actuation voltage levels to quantify the mean thrust resultant and power consumption levels for different aspect ratios. Variation of the thrust coefficient of the MFC bimorph fins with changing aspect ratio is also semi-empirically modeled and presented.

1 Introduction

The design of robotic fish exploiting smart materials has received growing interest in the last few years [1–12] for various potential applications of fish-like biomimetic locomotion ranging from underwater sensing and exploration for ecological monitoring and sustainability studies to drug delivery and disease screening in medicine [2, 13–15]. Among the commonly used smart materials (such as ionic polymer metal composites, shape memory alloys and piezoelectric materials as discussed in a recent review article [2]), Macro-Fiber Composites (MFCs) are effective piezoelectric actuators

^a e-mail: shima.shahab@gatech.edu

with the advantages of being light weight, flexible, durable, and available in various sizes. MFC actuators have been successfully used in tethered underwater robotic fish [16–18]. Employing MFCs in the design of untethered robotic fish [11] and bio-inspired thrust and power generation [10] has been proven to be fairly successful in our group. However, more research is required to investigate the effect of length-to-width (L/b) aspect ratio on the hydrodynamic thrust generation performance of MFC cantilever fins while accounting for the power consumption level during actuation.

Erturk and Delporte [10] investigated underwater thrust and power production using MFC bimorphs with and without a passive caudal fin. They [10] performed in-air and underwater base excitation experiments with an MFC-based fish-like propulsor with a caudal fin extension of the substrate. Comparing the in-air and underwater test results showed that the maximum underwater power output was an order of magnitude larger than its in-air counterpart for the same base acceleration level. Recently, an untethered piezoelectric robotic fish was developed by Cen and Erturk [11] with a swimming speed of 0.3 body length/second. In that work [11], electrohydroelastic dynamics of a fully submerged MFC bimorph propulsor was investigated for the theoretical and experimental analysis of fish-like aquatic robotics by accounting for the hydrodynamic effects presented in the papers by Sader et al. [19–22], which are based on two-dimensional fluid-structure interaction analysis for slender beams. Likewise, for underwater applications, Brunetto et al. [23], Mbemmo et al. [7], and Aureli et al. [8] used similar approaches to analyze the dynamics of ionic polymer-metal composite samples. The linear hydrodynamic function developed based on Sader's theory [19–22] assumes infinitesimal vibrations and a large length-to-width ratio. Therefore, as the vibration amplitude increases or length-to-width ratio decreases, the accuracy of Sader's theory is affected negatively [24,25]. Kopman and Porfiri [9] used Morison's nonlinear equation [26–30] to incorporate the effects of the surrounding fluid on caudal fins with different aspect ratios (Morison's equation was originally used to calculate fluid loading on a circular cylinder in viscous oscillatory flow). They [9] used a nonlinear hydroelastic model along with experimental thrust coefficients to calculate the resultant thrust of the beams. Facci et al. [31] compared the thrust coefficient for different values of oscillatory Reynolds numbers and aspect ratios by using 3D computational fluid dynamics simulations. They showed that, while the dependence of the thrust coefficient on the Reynolds number was relatively small and linear, there was a significant nonlinear dependence on the aspect ratio due to 3D fluid effects.

In the present paper, an experimentally validated nonlinear electrohydroelastic model for underwater resonant actuation of piezoelectric MFC cantilevers in quiescent water is developed based on the Euler-Bernoulli theory while incorporating the fluid effects using Morison's semi-empirical model [26,27] as in Kopman and Porfiri [9] and Cha et al. [32]. The inertia and drag coefficients in Morison's equation are experimentally identified by applying low input voltages for linear underwater actuation tests (resulting in both small deformations and small electric fields) [32,33]. Based on experimental data for the underwater vibration of passive aluminum plates and MFCs with different aspect ratios [33], a quadratic polynomial quotient curve fit is given for the dimensionless inertia coefficient. The electrohydroelastic model is used in conjunction with Lighthill's elongated-body theory to calculate the thrust production as a function of tip velocity and virtual mass (corrected with aspect ratio dependence) for quiescent water condition. Experiments are then conducted for various actuation voltage levels to quantify the mean thrust resultant and power consumption levels for different aspect ratios. The hydrodynamic thrust coefficient of the propulsor is estimated based on the virtual mass and aspect ratio, and then validated experimentally for MFC bimorphs with different aspect ratios.

2 Electrohydroelastic modeling

2.1 Underwater dynamics of a bimorph cantilever

Electrohydroelastically coupled equations for underwater actuation of an MFC cantilever bimorph (Fig. 1) can be expressed as follows:

$$D \frac{\partial^4 w(x, t)}{\partial x^4} + c_\alpha \frac{\partial^5 w(x, t)}{\partial x^4 \partial t} + c_\beta \frac{\partial w(x, t)}{\partial t} + m_s \frac{\partial^2 w(x, t)}{\partial t^2} + \Gamma(x, t) = \vartheta \left[\frac{d\delta(x)}{dx} - \frac{d\delta(x-L)}{dx} \right] v(t) \quad (1)$$

$$-i(t) + C_p \frac{dv(t)}{dt} + \vartheta \int_0^L \frac{\partial^3 w(x, t)}{\partial x^2 \partial t} dx = 0 \quad (2)$$

where D is the bending stiffness of the composite cross section, c_α and c_β are the stiffness-proportional and mass-proportional damping coefficients¹, respectively, m_s is the mass per unit length of the beam, L is the active overhang length, ϑ is the electro-mechanical coupling term, C_p is the capacitance, $\delta(x)$ is the Dirac delta function, $i(t)$ is the electrical current input (negative sign denotes current flow into the system), $v(t)$ is the actuation voltage input, and $w(x, t)$ is the transverse displacement (in z -direction). The electromechanical coupling term, ϑ , and capacitance, C_p , are obtained using the mixing rules formulation [34]. Furthermore, $\Gamma(x, t)$ is the hydrodynamic load per unit length due to the surrounding fluid (and L is the overall overhang length) and is expressed using Morison's semi-empirical equation as [9, 26, 27, 32]:

$$\Gamma(x, t) = \frac{\pi}{4} \rho_w b^2 c_m \frac{\partial^2 w(x, t)}{\partial t^2} + \frac{1}{2} \rho_w b c_d \frac{\partial w(x, t)}{\partial t} \left| \frac{\partial w(x, t)}{\partial t} \right| \quad (3)$$

where ρ_w is the mass density of water and b is the overall width of the bimorph. Moreover, c_m and c_d are the inertia and drag coefficients, respectively, which depend on the aspect ratio and are determined experimentally. Clearly, the damping component in Morison's equation introduces quadratic nonlinearity (unlike the classical linearized hydrodynamic function presented by Sader [19]), and therefore, in case of exploring multiple modes, vibration modes need to be explored separately as in [33]. Geometrically small oscillations and materially linear behavior are the main assumptions so that the only nonlinearity is due to hydrodynamic damping.

Assuming well separated modes (which is the case for bending modes of a uniform cantilever), the transverse deflection of the reference surface at position x and time t is

$$w(x, t) \cong \phi(x)\eta(t) \quad (4)$$

where $\phi(x)$ and $\eta(t)$ are the mass-normalized eigenfunction and the generalized modal coordinate for the fundamental vibration mode, respectively. The eigenfunction denoted by $\phi(x)$ is given for the transverse vibration of a clamped-free beam as

$$\phi(x) = \sqrt{\frac{1}{m_s L}} \left[\cos \frac{\lambda}{L} x - \cosh \frac{\lambda}{L} x + \frac{\sin \lambda - \sinh \lambda}{\cos \lambda + \cosh \lambda} \left(\sin \frac{\lambda}{L} x - \sinh \frac{\lambda}{L} x \right) \right] \quad (5)$$

¹ This combined generalized proportional damping form is assumed to account for the internal losses as a convenient mathematical representation.

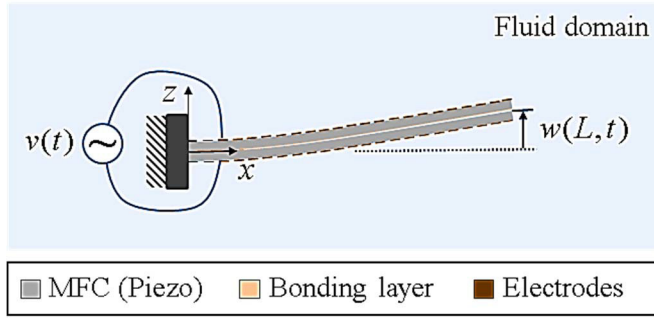


Fig. 1. Schematic representation of a bimorph cantilever under dynamic actuation in an unbounded quiescent fluid domain.

where $\lambda = 1.87510407$ and the expression given for $\phi(x)$ satisfies the orthogonality conditions as [11]:

$$\int_0^L m_s \phi^2(x) dx = 1 \quad (6)$$

$$\int_0^L \phi(x) D \frac{d^4 \phi(x)}{dx^4} dx = \omega_n^2 \quad (7)$$

where ω_n is the *in vacuo* undamped fundamental natural frequency and expressed as

$$\omega_n = \lambda^2 \sqrt{D/m_s L^4}. \quad (8)$$

Substituting the expression for $w(x, t)$ into Eqs. (1) and (2), multiplying by the mass normalized eigenfunction $\phi(x)$, integrating over the length of the beam, and applying the orthogonality conditions (Eqs. (6) and (7)) one obtains

$$(1 + \mu) \ddot{\eta}(t) + (2\zeta\omega_n + \gamma |\dot{\eta}(t)|) \dot{\eta}(t) + \omega_n^2 \eta(t) = \theta v(t) \quad (9)$$

$$-i(t) + C^{eq} \dot{v}(t) + \theta \dot{\eta}(t) = 0 \quad (10)$$

where $\mu = (\pi/4)(\rho_w b^2 c_m / m_s)$, $\gamma = (1/2)\rho_w b c_d \int_0^L \phi^2(x) |\phi(x)| dx$, and c_m and c_d are the inertia and drag coefficients for the fundamental vibration mode. Here $\theta = \vartheta \frac{d\phi(x)}{dx} \Big|_{x=L}$ is the modal electromechanical coupling term, C^{eq} is the equivalent capacitance of the bimorph cantilever, and ζ is the modal mechanical damping ratio. The modal electromechanical coupling and equivalent capacitance depend on the way the MFC laminates are wired. The analytical expressions for the equivalent capacitance and modal electromechanical coupling are given in [34] for the series and parallel connections of the MFC laminates.

To obtain the *in vacuo*² coupled mechanical and electrical equations, the hydrodynamic loading is set to zero such that $\mu = 0$ and $\gamma = 0$ in Eq. (9). For harmonic voltage excitation of the form $v(t) = V e^{j\omega t}$ (where ω is the excitation frequency and

² In the experiments of this paper, infinitesimal in-air vibration case will be used to approximate *in vacuo* condition so that the hydrodynamic load can be superimposed as in Eq. (1).

j is the unit imaginary number), assuming harmonic modal mechanical response of the form $\eta(t) = He^{j\omega t}$ and electrical current of the form $i(t) = Ie^{j\omega t}$, solving Eqs. (9) and (10) for the displacement frequency response function (FRF), $\alpha(\omega, x)$, yields

$$\alpha(\omega, x) = \frac{w(x, t)}{Ve^{j\omega t}} = \frac{\theta\phi(x)}{\omega_n^2 - \omega^2 + 2j\zeta\omega_n\omega}. \quad (11)$$

Note that the velocity FRF can be obtained through multiplying $\alpha(\omega, x)$ by $j\omega$ for harmonic response of the cantilever bimorph.

The method of harmonic balance is used to analyze periodic solutions of nonlinear ordinary Eqs. (9) and (10). Using this method, a Fourier series solution is assumed and the ordinary differential equations are replaced with algebraic equations (the details of harmonic balance analysis can be found elsewhere [35–37]). In this work, a single-term harmonic balance solution is adequate for approximating the steady-state response to harmonic input voltage.

The input voltage, $v(t)$, is harmonic of the form

$$v(t) = V \cos \omega t. \quad (12)$$

The unknown modal coordinate $\eta(t)$ and the current flow through the piezoelectric bimorph, $i(t)$, are assumed to be of the form:

$$\eta(t) = H_0 \cos \omega t + H_1 \sin \omega t \quad (13)$$

$$i(t) = I_0 \cos \omega t + I_1 \sin \omega t. \quad (14)$$

Substituting Eqs. (12)–(14) into Eqs. (9) and (10) and using the harmonic balance method yield the following set of algebraic equations in H_0 , H_1 , I_0 , and I_1 for the first vibration mode.

$$-(1 + \mu)\omega^2 H_0 + (2\zeta\omega_n + \frac{8}{3\pi}\gamma\omega\sqrt{H_0^2 + H_1^2})\omega H_1 + \omega_n^2 H_0 - \theta V = 0 \quad (15)$$

$$-(1 + \mu)\omega^2 H_1 - (2\zeta\omega_n + \frac{8}{3\pi}\gamma\omega\sqrt{H_0^2 + H_1^2})\omega H_0 + \omega_n^2 H_1 = 0 \quad (16)$$

$$-I_0 + \theta\omega H_1 = 0 \quad (17)$$

$$I_1 + C^{eq}\omega + \theta\omega H_0 = 0. \quad (18)$$

The coefficient γ in Eqs. (15) and (16) is obtained by evaluating the integral using 61 Gaussian quadrature points at given excitation frequency. The resulting system of algebraic equations (Eqs. (15–18)) is solved numerically using the “solve” function in MATLAB®. The numerical solution with the default algorithm (trust-region dogleg) is attempted by the solve function and the default tolerance of 10^{-6} is used.

2.2 Hydrodynamic mean thrust and identification of the thrust coefficient based on Lighthill’s theory of elongated-body propulsion

Lighthill’s model [40–43] is applied in the present work to estimate the mean thrust in quiescent water. Lighthill’s elongated-body theory [43] is based on the reactive forces

between the virtual mass of the surrounding fluid and the vibrating slender body. The mean thrust, T , produced by the cantilever MFC bimorph is calculated as

$$T = \frac{1}{2}m_v \left[\overline{\left(\frac{\partial w(x,t)}{\partial t}\right)^2} - U^2 \overline{\left(\frac{\partial w(x,t)}{\partial x}\right)^2} \right]_{x=L} \quad (19)$$

where U is relative speed of external free stream (or the swimming speed of propulsor) which is neglected for quiescent water conditions (i.e. $U \rightarrow 0$ is assumed as an approximation). The overbar denotes the mean values for the time derivative and the spatial derivative of the transverse deflection, $w(x,t)$, and m_v is the virtual mass at $x = L$ which is estimated as

$$m_v = \frac{\pi \rho_w b^2}{4} c_m. \quad (20)$$

In most instances of thrust calculation using Lighthill's theory [6,7,11], the virtual mass coefficient (equivalent to the inertia coefficient used in Eq. (3), cf. Eqs. (3) and (20)), c_m , is taken as unity based on two-dimensional fluid-structure analysis for slender beams [19,44]. The current analysis utilizes accurate values of the virtual mass coefficient to calculate the thrust stemming from the actuation of various MFC bimorphs with differing aspect ratios. To identify c_m [24,25], each MFC bimorph is clamped and tested for actuation both in air and under water. The in-air and underwater experimental FRFs are correlated with model simulations (based on the analysis explained in Sect. 2.1) that used only experimental parameters for the identification of the inertia coefficients of the fundamental mode, and are then used in the semi-empirical electrohydroelastic Euler-Bernoulli-Morison model for experimental validations. Figure 2 displays the identified hydrodynamic virtual mass coefficient (c_m values for different aspect ratios are determined experimentally) focusing on the first bending mode for both mechanically base-excited aluminum cantilevers and electrically actuated MFC cantilevers with different aspect ratios ($\psi = L/b$). The experimental vibration characteristics of the aluminum strips considered in this study are explained in detail by Shahab and Erturk [25]. It is observed that c_m shows asymptotic behavior for ψ greater than approximately 5 and becomes insensitive to ψ (the cases of ψ smaller than 5 are sensitive to aspect ratio). Specifically, in Fig. 2, $c_m(\psi)$ converges to unity for large ψ in agreement with predictions of classical flow solutions for the two dimensional fluid-structure problem in which the linear hydrodynamic forces are dominant [19,45]. The repeatability of c_m is observed for samples with the same aspect ratio [33], and curve fit expressions are reported for inertia coefficients. The following quadratic curve fitting polynomial quotient, determined using the curve fitting toolbox within MATLAB[®] is given for the dimensionless parameter c_m for the first bending mode.

$$c_m = \frac{\psi^2 - 0.701\psi + 0.374}{\psi^2 - 1.111\psi + 2.637}. \quad (21)$$

3 Experimental validations

3.1 Details of experimental setup

Three MFC bimorphs are formed by bonding pairs of MFCs of different aspect ratios (M8528-P1, M8514-P1, and M8507-P1 from the Smart Material Corporation [46], shown in Fig. 3a) using high shear strength epoxy and a vacuum bonding process

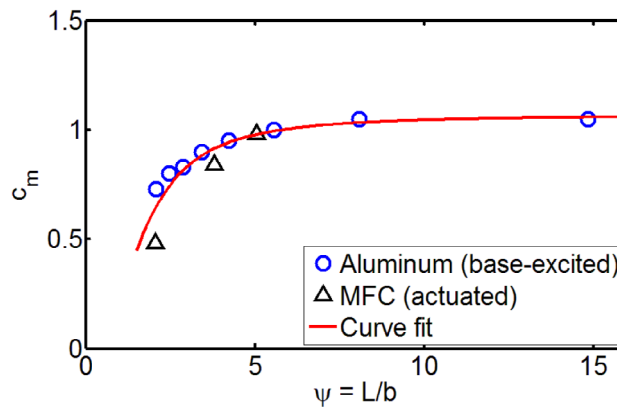


Fig. 2. Hydrodynamic inertia coefficient (c_m) vs. aspect ratio (ψ) for the fundamental bending mode.

Table 1. Geometric and structural properties of the MFC bimorphs (L : overhang length, b : width, h : total thickness, m_s : structural mass per length).

	L (mm)	b (mm)	h (mm)	m_s (kg m^{-1})
	[active*, overall]	[active, overall]		
M8507-P1	[75.5, 85.5]	[7, 16.5]	0.61	0.028
M8514-P1	[75.5, 83.5]	[14, 21.5]	0.61	0.045
M8528-P1	[75.5, 90.6]	[28, 43.5]	0.61	0.075

* Active length and width define the portions which are covered with piezoelectric material.

(described elsewhere [47]). Table 1 summarizes the physical properties of the MFC bimorphs. The MFC pairs are wired in parallel in all cases, and the equivalent capacitances of the bimorphs are measured experimentally via a capacitance meter. These three bimorphs are rigidly clamped at one end (shown in Fig. 3b) and linearly actuated in-air with a low-voltage sinusoidal input. The actuation voltage signal is generated by a National Instruments NI USB-4431 card and amplified using a power amplifier (Trek, Inc. Model 2220). Actuation voltage and current data are collected from the amplifier, as well as tip velocity measurements from a laser Doppler vibrometer (LDV, Polytec PDV 100) and recorded using the NI USB-4431 module.

To measure the hydrodynamic mean thrust, each sample is attached to the free end of a fixed-free $254 \text{ mm} \times 25.4 \text{ mm} \times 6.35 \text{ mm}$ elastic aluminum transducer cantilever and submerged under water, as seen in Figs. 3c and d. The deflection of the aluminum cantilever in response to thrust resultant of each sample during actuation is measured by an optical displacement sensor (Micro-Epsilon optoNCDT 2300-50), as shown in Fig. 3d, and the thrust force is extracted using the calibration curve seen in Fig. 4, as explained next.

The hydrostatic pressure effects cancel out in the underwater experiments, so the mean thrust is assumed to be a point force applied to the transducer cantilever through the center of the clamp holding the MFC, which results in a deflection of the free end of the transducer cantilever. The transducer cantilever is calibrated horizontally and in air, where weights are gradually added to the location of the point force with the aid of gravity while the static displacement of the free end of the transducer is measured. The resulting calibration curve, shown in Fig. 4, is determined to be linear for the range of deflections seen in these experiments. Since the stiffness of the

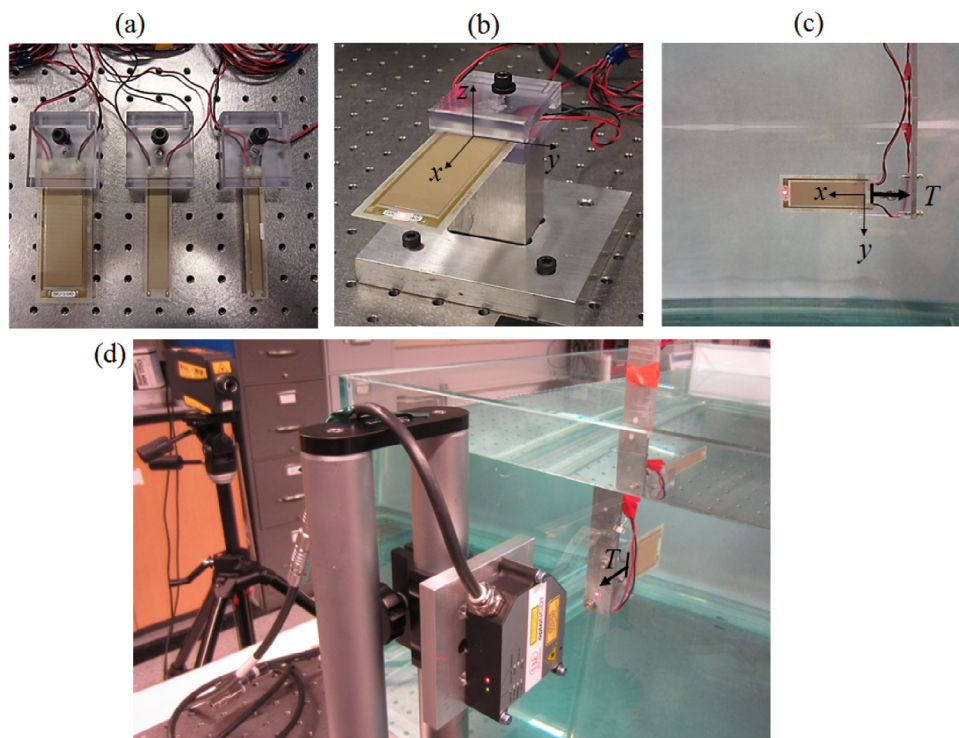


Fig. 3. (a) Clamped MFC bimorphs (from left to right: M8528-P1, M8514-P1, and M8507-P1), (b) in-air dynamic actuation test setup, (c) side view of the underwater configuration of the MFC bimorph for the measurement of its tip velocity-to-actuation voltage FRF and (d) front view of underwater configuration of MFC bimorph for mean thrust measurement.

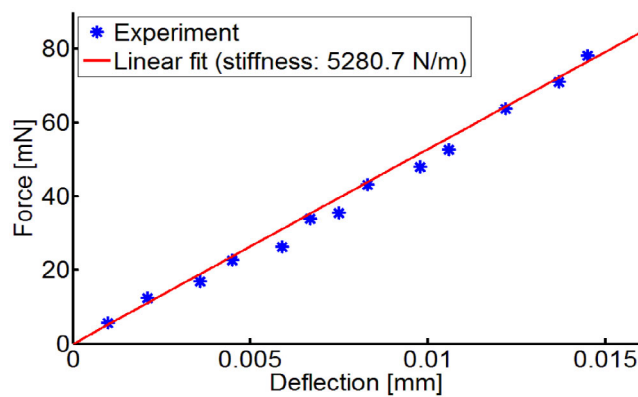


Fig. 4. Linear calibration curve for the aluminum transducer cantilever to relate constrained mean head displacement to mean thrust.

transducer cantilever is unchanged in air and under water, the in-air calibration can be utilized for the underwater experiments as in Cen and Erturk [11]. Impact hammer testing is performed on this transducer cantilever to ensure that the first mode of the transducer is well separated from the first mode of the MFC bimorphs, both in air and under water.

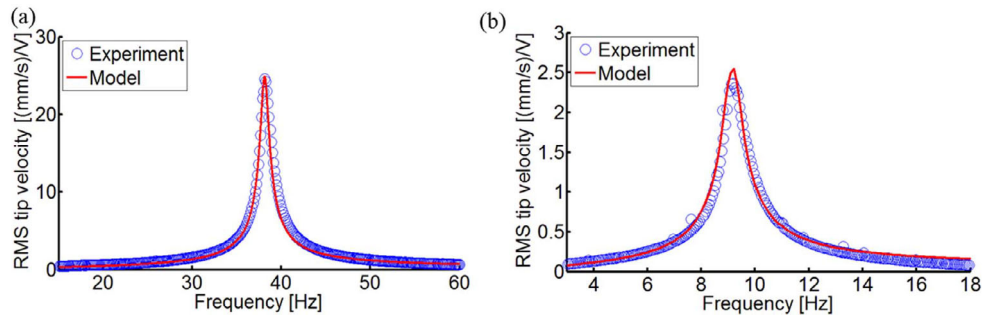


Fig. 5. (a) In-air and (b) underwater experimental and analytical tip velocity FRF for M8528-P1.

3.2 In-air and underwater velocity FRFs and parameter identification

Tip velocity-to-actuation voltage FRFs for in-air and underwater actuation experiments and model results for M8528-P1 are shown in Figs. 5a and b, respectively. For brevity, the results for the remaining samples are not graphically presented here. During the actuation experiments, low-voltage harmonic excitation is applied, resulting in a linear response. The identified parameters based on the in-air actuation experiments are summarized in Table 2. The bending stiffness, D , is identified by using the experimental fundamental resonance frequency of the bimorph. The damping ratio, ζ , is obtained by using the half-power-point method [48]. The identified modal electromechanical coupling term, θ , for each sample is in agreement with the predicted values obtained using the mixing rules formulation (for the parallel wiring of MFC laminates) presented by Shahab and Erturk [34]. The equivalent capacitance, C^{eq} , of each bimorph is measured experimentally.

Once the analytical model for in-air actuation of the bimorphs is validated (using Eq. (11) in Fig. 5a) and the parameters are identified, three case studies are tested and analyzed (using Morison's hydrodynamic function) for linear underwater actuation. As previously explained in Sect. 2, in-air and underwater experimental FRFs are correlated with model simulations based on purely experimental parameters for accurate identification of the first mode inertia and drag coefficients (e.g. the inertia coefficients are given in Fig. 2) [34]. The correlation is done by using the built-in "fit" function in MATLAB[®] for the experimental data. Specifically, the inertia coefficient, c_m , can be obtained by correlating the resonance frequency of the model to the experimental data. The monotonic increase of coefficients c_m and c_d with respect to aspect ratio with an asymptotic trend for large aspect ratios was shown in Fig. 9 in [34]. In that work [34], the authors presented curve fitting polynomial ratio expressions for the dimensionless inertia and drag coefficients as a function of the aspect ratio. These drag and inertia coefficients, when used in the semi-empirical electrohydroelastic Euler-Bernoulli-Morison model, result in the underwater FRF prediction given in Fig. 5b.

The c_m values used in this work are 0.069, 0.91, and 1.02 for length-to-width aspect ratios of $\psi = 2.1$, 3.9, and 5.4, respectively. These coefficients are consistent with what is presented in Fig. 2 and Eq. (21). In this work, Lighthill's slender-body theory [40,41] is used to predict the thrust output in quiescent water by reducing Lighthill's mean thrust expression to quiescent water condition.

It is important to note that the electrohydroelastic model given in Sect. 2 is valid only for excitations around the fundamental natural frequency since higher vibration modes are not used in Eqs. (15)–(18). In addition, the derivation neglects the

Table 2. Experimentally identified parameters from in-air actuation experiments.

	M8507-P1	M8514-P1	M8528-P1
f_{sc} (Hz)	35.5	46.4	38.1
D (N m ²)	0.0045	0.0101	0.0125
ζ (%)	1.6	1.8	1.3
θ (10 ⁻³ C/m√kg)	4.5	7.5	10
C^{eq} (nF)	5.5	6.7	19.3

geometric, material, and internal dissipative nonlinearities [49–51]. Therefore, the geometrically and materially linear model predictions would fail under high actuation voltage levels (e.g. peak-to-peak voltage input: 400 V to 800 V) due to geometric and electroelastic nonlinearities [49–51]. Modeling of MFC dynamics under high voltage actuation and incorporating hydrodynamic effects [52] in such a nonlinear model are of interest for future work.

3.3 Mean thrust and tip velocity correlation, and power consumption analysis

The experimental tip velocity and mean thrust measurements for the M8528-P1 bimorph are shown in the frequency range of 1–11 Hz, which captures the resonance frequency of the bimorph for peak-to-peak actuation voltage levels of 400, 600, and 800 V (Figs. 7a and b). For a given actuation frequency and amplitude, the bimorphs were excited as per Fig. 6a, where there is 10 seconds of pre-actuation where no voltage is applied, then 10 seconds of a sinusoidal voltage input at the given frequency and amplitude, and finally 10 seconds of post-actuation where there is again no input voltage. The tip velocity of the bimorph, displacement of the transducer cantilever, input voltage and current for the bimorph were measured as the bimorph is excited, and subsections where the response of the bimorph is in quasi-steady state during the pre-actuation, actuation, and post-actuation phases are extracted from the time histories. These quasi-steady state subsections are used to determine the RMS tip velocity, mean thrust, RMS current, and mean power consumed for each actuation frequency and amplitude. The mean displacement of the transducer cantilever caused by the thrust is the difference between the mean value during actuation and the average of the mean values during the pre-actuation and post-actuation phases. Figure 6 shows a representative time trace of input actuation voltage, transverse tip velocity, and transducer cantilever displacement in the direction of positive thrust (in Figs. 3c and d) during pre-actuation, actuation, and post-actuation phases at 5.5 Hz under a peak-to-peak input actuation voltage of 800 V.

The analytical thrust curves shown in Fig. 7b use Lighthill’s theory for a bimorph propulsor in quiescent water conditions based on the measured tip velocity shown in Fig. 7a. For M8528-P1 ($\psi = 2.1$), M8514-P1 ($\psi = 3.9$), and M8507-P1 ($\psi = 5.4$), the inertia coefficients (c_m) in Eq. (20) are defined as 0.069, 0.91, and 1.02, respectively, based on the semi-empirical Euler-Bernoulli-Morison electrohydroelastic analysis presented in Sect. 2 and plotted in Fig. 2. It should be noted that, the inertia coefficient is estimated close to unity when the linear hydrodynamic forces are dominant on the predictions of classical flow solutions of the two-dimensional fluid-structure problem [19], whereas recent experimental and analytical data presented by Cha et al. [32] and Shahab and Erturk [24, 25] show that the inertia coefficient is controlled by the aspect ratio, especially for $\psi < 5$.

The experimental current amplitude and average power plots for the MFC bimorph at various actuation frequencies and voltages are shown in Figs. 7c and d. The data obtained for the thrust and power consumption is used later to analyze the effect

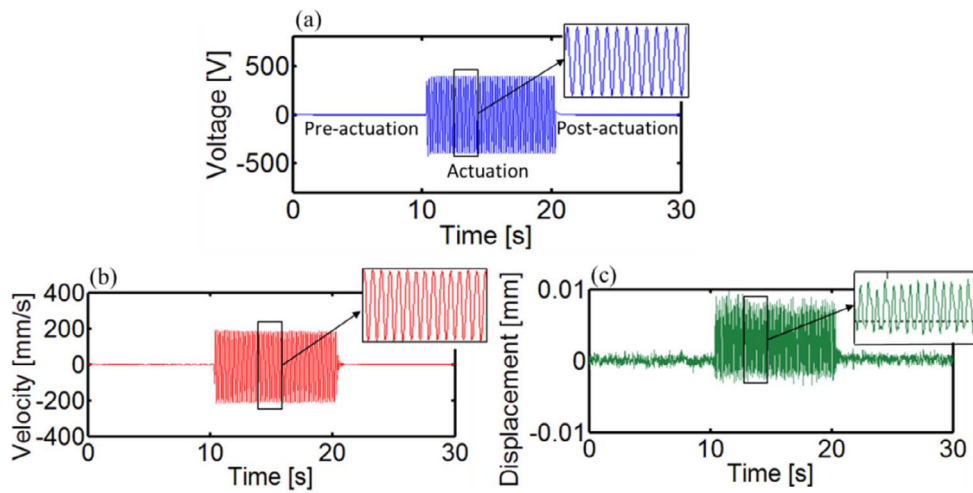


Fig. 6. Representative time trace of (a) input actuation voltage, (b) measured transverse tip velocity, and (c) head displacement during pre-actuation, actuation, and post-actuation at 5.5 Hz.

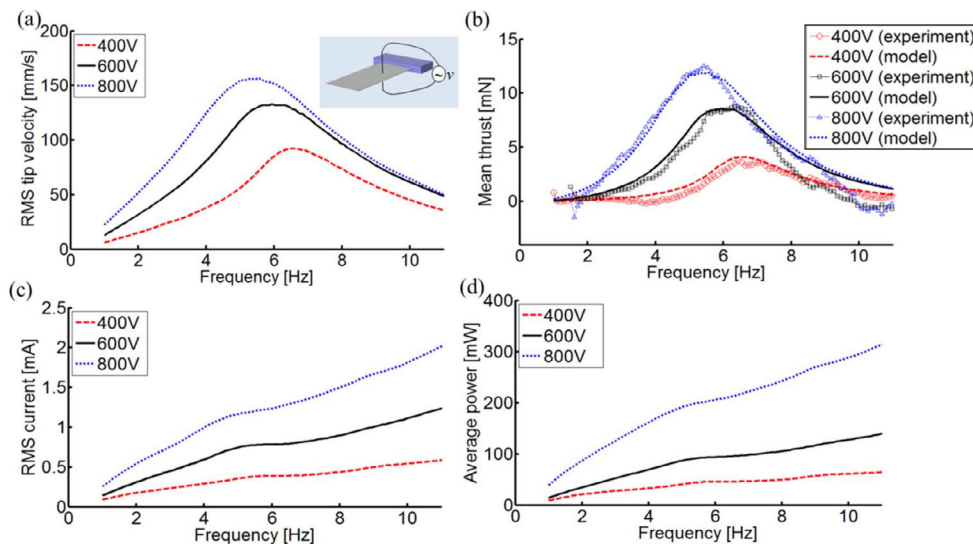


Fig. 7. (a) Experimental tip velocity, (b) measured and predicted thrust curves, (c) experimental current input, and (d) average power input curves for M8528-P1 ($\psi = 2.1$) under different actuation voltage levels.

of aspect ratio on the thrust generated per power input. In Fig. 7b, the agreement between the experimental thrust measurements and the model validates the use of the reduced form of Lighthill's theory [40, 41] (which uses the measured tip velocity and predicted virtual mass by the Euler-Bernoulli-Morison electrohydroelastic model) for the bimorph under three different high-level input voltages.

Next, Lighthill's theory is employed for two more case studies with larger aspect ratios where the thrust levels, which are prone to noise, are difficult to accurately

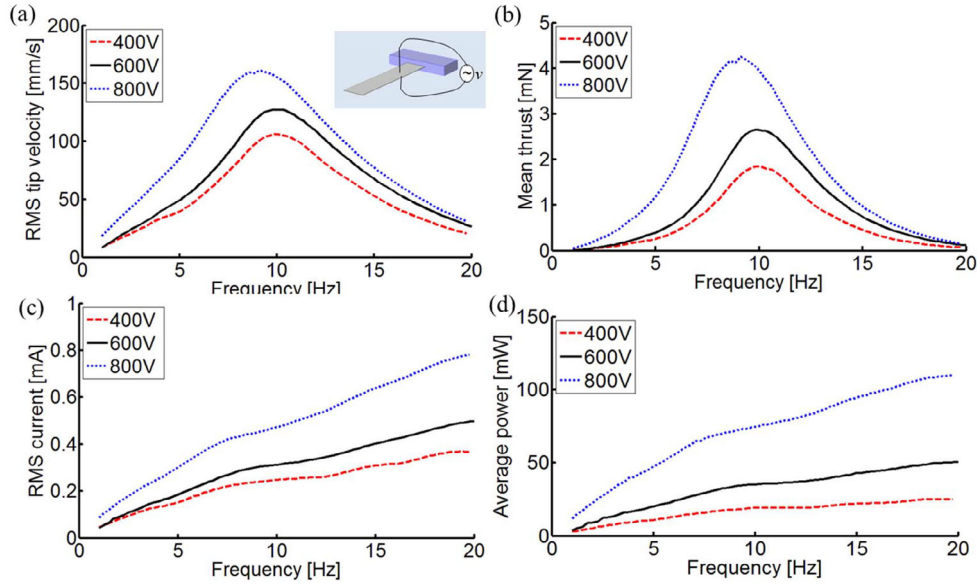


Fig. 8. (a) Experimental tip velocity, (b) predicted thrust curves, (c) experimental current input, and (d) average power input curves for M8514-P1 ($\psi = 3.9$) under different actuation voltage levels.

measure experimentally. In each case, the correlation between measured tip velocity and predicted thrust shows that the thrust levels increase with increasing tip velocities, as expected. Figures 8a and 9a show the experimentally determined RMS tip velocity for the higher aspect ratio bimorphs under varying actuation frequencies and voltages, and Figs. 8b and 9b show the corresponding predicted thrust curves. In Figs. 7, 8 and 9c,d, the current amplitude and average power plots for different actuation frequencies and voltages are given.

The ratio, Φ , between the mean thrust (obtained using Lighthill's theory for the measured tip velocity for 800 V peak-to-peak input voltage) and the average power consumption for the three aspect ratios is shown in Fig. 10a. Figures 7a, 8a and 9a show that at resonant frequencies, the magnitudes of the tip velocities between the three samples are comparable. However, the MFC bimorph with largest aspect ratio has the least added mass, resulting in a lower power consumption level for the same tip velocity as compared to the other two samples. For example, Figs. 7d, 8d and 9d show that the average power consumption for the sample with $\psi = 5.4$, is approximately 2 times less than that of the sample with $\psi = 3.9$, and approximately 5 times less than the sample with $\psi = 2.1$ around the resonant frequencies for 800 V input actuation voltage. At the same time, the thrust levels generated by the bimorph cantilevers are dominantly proportional to the square of their widths (based on Eqs. (19) and (20)), and considering the dependence of thrust on inertia coefficient). The sample with largest aspect ratio ($\psi = 5.4$) produces the least thrust, as can be observed in Figs. 7b, 8b and 9b. Combining these two effects, the maximum mean thrust resultant to average power consumption level for the three MFC bimorphs is approximately a constant average value of 60.7 mN/W, as presented in Fig. 10b. However, it is observed in Fig. 10a that the samples with larger aspect ratios maintain their response in a broader frequency range (due to higher drag coefficient [34]), which might be

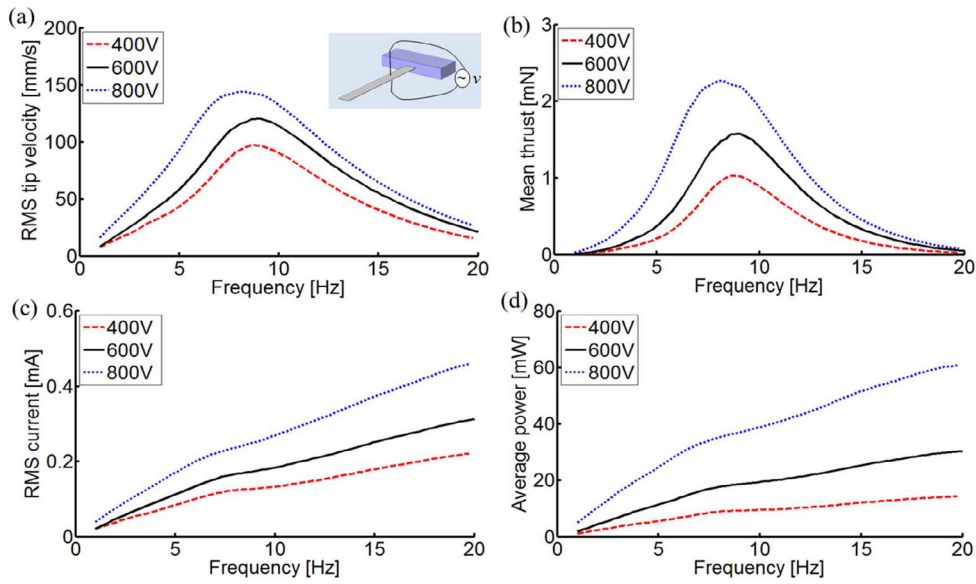


Fig. 9. (a) Experimental tip velocity, (b) predicted thrust curves, (c) experimental current input, and (d) average power input curves for M8507-P1 ($\psi = 5.4$) under different actuation voltage levels.

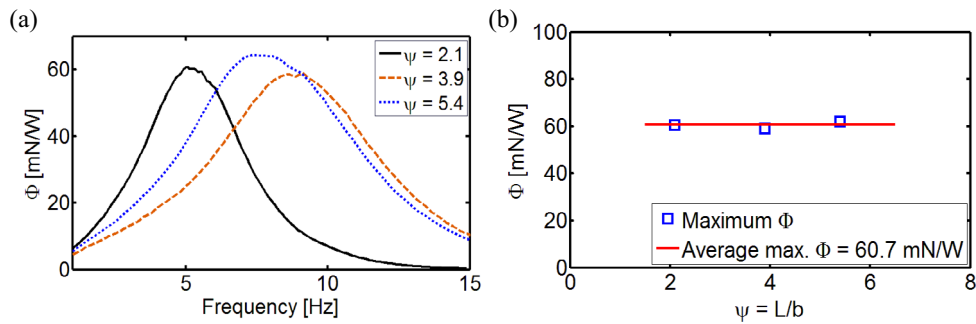


Fig. 10. (a) Mean thrust to power consumption ratio for three aspect ratios (800 V peak-to-peak input voltage) and (b) maximum mean thrust to average power consumption ratio vs. aspect ratio.

of interest for future design purposes to have less sensitivity to frequency variations around resonance.

3.4 Identification of the thrust coefficient

In order to study the effects of the cantilever geometry, oscillation frequency, and tip displacement amplitude on the resultant thrust with a compact expression, the non-dimensional thrust coefficient, c_τ , is defined as [53]

$$c_\tau = \frac{T}{\frac{1}{2}\rho_w\omega^2|w(L,t)|^2bL}. \quad (22)$$

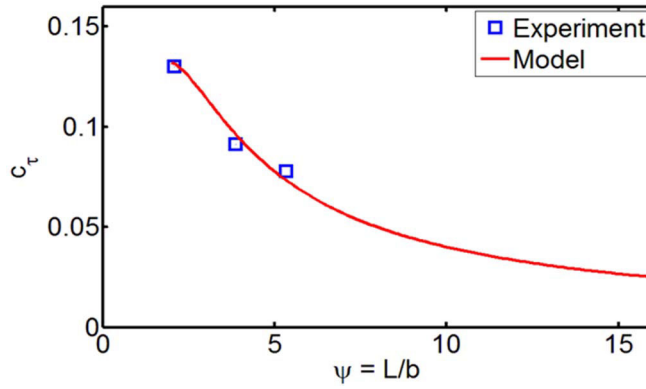


Fig. 11. Identified experimental and semi-empirical Euler-Bernoulli-Morison model curve of thrust coefficient vs. aspect ratio (ψ).

Substituting Eqs. ((19)–(20)) into Eq. (22) yields an expression for c_τ in terms of the inertia coefficient, c_m . Combining this expression with the expression given in Eq. (21) results in an expression for c_τ as a function of the length-to-width aspect ratio, ψ :

$$c_\tau = 0.393 \frac{c_m}{\psi} = \frac{0.393\psi^2 - 0.275\psi + 0.147}{\psi^3 - 1.111\psi^2 + 2.637\psi} \quad (23)$$

Figure 11 displays the experimental thrust coefficients of the actuated MFC cantilevers with different aspect ratios ($\psi = L/b$) along with the curve obtained from Eq. (23). By increasing ψ , the thrust coefficient is significantly reduced with this nonlinear dependence on aspect ratio, which is attributed to the reduction of the overall fluid loading on the structure. This observation is consistent with the results reported by Facci et al. [31] (Fig. 7 in [31]) through 3D computational fluid dynamics simulations that investigate the effects of aspect ratio on the thrust production from vibration of a thin cantilever plate submerged in fluid.

4 Conclusions

Bio-inspired thrust generation using piezoelectric transduction is investigated theoretically and experimentally for MFC bimorphs with different length-to-width aspect ratios. In an effort to develop electrohydroelastic models for these cantilevers, the present work studied MFC bimorphs with three different aspect ratios for small amplitude bending vibrations under piezoelectric actuation. In-air experiments were conducted for model validation and for the characterization of the bimorph propulsors. Underwater tip velocity FRFs were then derived by combining their in-air counterparts with Morison's nonlinear hydrodynamic function. The inertia and drag coefficients in Morison's equation were identified experimentally. The hydrodynamic effects added to the electroelastic in-air model successfully represent the underwater dynamics for small oscillations. However, high actuation voltage levels during the experiments that included thrust measurements cause nonlinear electrohydroelastic behavior due to electroelastic, geometric, and dissipative nonlinear effects. For future work, accounting for nonlinear electroelastic dynamics [49–51] along with nonlinear hydrodynamic effects [52] is required to predict the dynamics of the propulsor for large oscillations and strong electric fields. In this work, the experimentally obtained vibration response and the inertia coefficient (defined in Morison's hydrodynamic

function) are coupled with Lighthill's elongated-body theory [40,41] to predict the thrust output. Although the inertia and drag coefficients were found to be highly dependent on the aspect ratio for $\psi < 5$, the maximum mean thrust to power consumption ratio is found to be insensitive to the aspect ratio, which may influence the future design of untethered biomimetic robotic fish using MFCs. It is also noted that the thrust output per power input frequency response has increased bandwidth for increased length-to-width aspect ratio (due to increased drag coefficient). Variation of the thrust coefficient of the MFC bimorph fins with changing aspect ratio is also semi-empirically modeled and presented.

This work was supported in part by the NSF Grant CMMI-1254262.

References

1. B. Kim, D.-H. Kim, J. Jung, J.-O. Park, *Smart Mater. Struct.* **14**, 1579 (2005)
2. W.-S. Chu, K.-T. Lee, S.-H. Song, M.-W. Han, J.-Y. Lee, H.-S. Kim, M.-S. Kim, Y.-J. Park, K.-J. Cho, S.-H. Ahn, *Int. J. Precision Eng. Manuf.* **13**, 1281 (2012)
3. X. Tan, D. Kim, N. Usher, D. Laboy, J. Jackson, A. Kapetanovic, J. Rapai, B. Sabadus, X. Zhou, *Intell. Robots Syst., IEEE/RSJ Int. Conf. IEEE* (2006)
4. X. Ye, Y. Su, S. Guo, *Robotics Biomimetics, ROBOT 2007. IEEE Int. Conf. IEEE* (2007)
5. X. Ye, Y. Su, S. Guo, L. Wang, *In Adv. Intell. Mechatronics, AIM 2008. IEEE/ASME Int. Conf. IEEE* (2008)
6. Z. Chen, S. Shatara, X. Tan, *Mechatronics, IEEE/ASME Trans.* **15**, 448 (2010)
7. E. Mbemmo, Z. Chen, S. Shatara, X. Tan, *Robotics Automation, ICRA 2008. IEEE Int. Conf. IEEE* (2008)
8. M. Aureli, V. Kopman, M. Porfiri, *Mechatronics, IEEE/ASME Trans.* **15**, 603 (2010)
9. V. Kopman, M. Porfiri, *Mechatronics, IEEE/ASME Trans.* **18**, 471 (2013)
10. A. Erturk, G. Delporte, *Smart Mater. Struct.* **20**, 125013 (2011)
11. L. Cen, A. Erturk, *Bioinspiration Biomimet.* **8**, 016006 (2013)
12. Z. Wang, G. Hang, J. Li, Y. Wang, K. Xiao, *Sensors Actuators A: Phys.* **144**, 354 (2008)
13. P.R. Byopadhyay, *Oceanic Eng., IEEE J.* **30**, 109 (2005)
14. D. Roper, S. Sharma, R. Sutton, P. Culverhouse, *Proc. Inst. Mech. Eng., Part M: J. Eng. Maritime Envir.* **225**, 77 (2011)
15. O. Barannyk, B.J. Buckham, P. Oshkai, *J. Fluids Struct.* **28**, 152 (2012)
16. Y. Nagata, S. Park, A. Ming, M. Shimojo, *Adv. Intell. Mechatronics, AIM 2008. IEEE/ASME Int. Conf. IEEE* (2008)
17. A. Ming, S. Park, Y. Nagata, M. Shimojo, *Robotics Automation, ICRA'09. IEEE Int. Conf. IEEE* (2009)
18. J. Shintake, A. Ming, M. Shimojo, *Intell. Robots Syst. (IROS), IEEE/RSJ Int. Conf. IEEE* (2010)
19. J.E. Sader, *J. Appl. Phys.* **84**, 64 (1998)
20. C.A. Van Eysden, J.E. Sader, *J. Appl. Phys.* **101**, 044908 (2007)
21. J.W. Chon, P. Mulvaney, J.E. Sader, *J. Appl. Phys.* **87**, 3978 (2000)
22. C.A. Van Eysden, J.E. Sader, *J. Appl. Phys.* **100**, 114916 (2006)
23. P. Brunetto, L. Fortuna, S. Graziani, S. Strazzeri, *Smart Mater. Struct.* **17**, 025029 (2008)
24. S. Shahab, A. Erturk, *SPIE Smart Struct. Mater.+ Nondestructive Evaluation Health Monitoring. Int. Soc. for Optics Photonics* (2014)
25. Shahab, S. Erturk, A. ASME 2014 Conf. Smart Mater., Adaptive Struct. Intell. Syst. Amer. Soc. Mech. Eng. (2014)
26. J. Morison, J. Johnson, S. Schaaf, *J. Pet. Technol.* **2**, 149 (1950)
27. J. Morison, J.W. Johnson, M.P. O'Brien, *Coastal Eng. Proc.* **1**, 25 (1953)
28. J. Graham, *J. Fluid Mech.* **97**, 331 (1980)
29. T. Sarpkaya, *J. Fluid Mech.* **165**, 61 (1986)

30. E. Tuck, *J. Eng. Math.* **3**, 29 (1969)
31. A.L. Facci, M. Porfiri, *J. Fluids Struct.* **38**, 205 (2013)
32. Y. Cha, H. Kim, M. Porfiri, *Smart Mater. Struct.* **22**, 115026 (2013)
33. S. Shahab, A. Erturk, *SPIE Smart Struct. Mater.+ Nondestructive Evaluation Health Monitoring. Int. Soc. Optics Photonics* (2015)
34. S. Shahab, A. Erturk, *Proc. ASME 2015 IDETC 27th Biennial Conf. Mech. Vib. Noise, Boston, MA*, **2** August (2015)
35. A.H. Nayfeh, *Perturbation methods* (John Wiley & Sons, 2008)
36. S. Leadenham, A. Erturk, *J. Sound Vib.* **333**, 6209 (2014)
37. S. Leadenham, A. Erturk, *Nonlinear Dyn.* (in press) (2014)
38. G. Taylor, *Proc. Royal Soc. Lond Ser. Math. Phys. Sci.* **209**, 447 (1951)
39. G. Taylor, *Proc. Royal Soc. Lond Ser. A. Math. Phys. Sci.* **211**, 225 (1952)
40. M. Lighthill, *J. Fluid Mech.* **9**, 305 (1960)
41. M. Lighthill, *Ann. Rev. Fluid Mech.* **1**, 413 (1969)
42. L. Cen, Fish-like locomotion using flexible piezoelectric composites for untethered aquatic robotics, *Georgia Inst. Technol.* (2012)
43. M.L. Hill, *J. Fluid Mech.* **44**, 256 (1970)
44. M. Lighthill, *J. Fluid Mech.* **44** 265
45. W. Chu, DTMB, Contract NObs-86396 (X), Southwest Res. Inst., San Antonio, Texas (1963)
46. <http://www.smart-material.com/>
47. S. Anton, A. Erturk, D. Inman, *Smart Mater. Struct.* **19**, 115021 (2010)
48. L. Meirovitch, *Fundamentals Vib.* (Wavel Press, 2010)
49. K. Wolf, O. Gottlieb, *J. Appl. Phys.* **91**, 4701 (2002)
50. T. Usher, A. Sim, *J. Appl. Phys.* **98** (2005)
51. S.C. Stanton, A. Erturk, B.P. Mann, E.H. Dowell, D.J. Inman, *J. Intell. Mater. Syst. Struct.* **23**, 183 (2012)
52. M. Aureli, M.E. Basaran, M. Porfiri, *J. Sound Vib.* **331**, 1624 (2012)
53. K. Abdelmour, E. Mancia, S.D. Peterson, M. Porfiri, *Smart Mater. Struct.* **18**, 085006 (2009)